High-index Faceted RuCo Nanoscrews for Water Electrosplitting

Ting Zhu, Ju Huang, Bolong Huang, Nan Zhang, Shangheng Liu, Qing Yao, Shu-Chih Haw, Yu-Chung Chang, Chih-Wen Pao, Jin-Ming Chen, Qi Shao, Zhiwei Hu, Yanhang Ma, and Xiaoqing Huang**

T. Zhu, N. Zhang, S. Liu, Q. Yao, Q. Yao, Prof. X. Huang
College of Chemistry, Chemical Engineering and Materials Science, Soochow University, Jiangsu 215123, China.
E-mail: hxq006@suda.edu.cn

T. Zhu, Prof. X. Huang
College of Chemistry and Chemical Engineering, Xiamen University, Xiamen 361005, China.
E-mail: hxq006@xmu.edu.cn

Dr. S. Haw, Dr. Y. Chang, Dr. C. Pao, Prof. J. Chen
National Synchrotron Radiation Research Center, Hsinchu, 30076, Taiwan.

Prof. Z. Hu
Max-Planck-Institute for Chemical Physics of Solids, Nöthnitzer Street, 4001187, Dresden, Germany.

J. Huang, Prof. Y. Ma
School of Physical Science and Technology, ShanghaiTech University, Shanghai 201210, China.

Prof. B. Huang
Department of Applied Biology and Chemical Technology, The Hong Kong Polytechnic University, Hung Hom, Kowloon, Hong Kong SAR 999077, China.
E-mail: bhuang@polyu.edu.hk

Keywords: Water splitting, Nanoscrew, High-index facet, Low-coordination structure, Shape control synthesis

The shape control has realized huge success for developing efficient Pd/Pt-based nanocatalysts, but the control of Ru-based nanocrystals remains formidable challenging due to the inherent anisotropy in hexagonal closed-packed nanocrystals. Herein, a class of unique RuCo nanoscrews (NSs) for water electrosplitting has been successfully synthesized with rough surfaces and the exposure of steps and edges. Those high-index faceted RuCo NSs show superior performances for overall water electro-splitting, where a low cell voltage of 1.524 V (@ 10 mA cm^{-2}) and excellent stability for more than 20 h (@ 10 mA cm^{-2}) for overall water electrosplitting in 1 M KOH has been achieved. The enhanced performance of

RuCo NSs is due to the optimization of the binding energy with the intermediate species and the reduced energy barrier of water dissociation. Density functional theory (DFT) calculations reveal that, the RuCo NS structure intrinsically endows various ridges and edges, which create amounts of extraordinarily low coordinated Ru- and Co- sites. These active Ru- and Co- sites present high efficiencies in electronic exchange and transfer (EXT) between adsorbing O species and nearby lattice sites, guaranteeing the high H_2O-splitting activities. This present work opens up a new strategy for creating high-performance electrocatalysts for water splitting.

Hydrogen energy, due to its high gravimetric energy density, has been recognized as an ideal alternative for fossil energy[1]. Electrochemical water splitting, as an effective method for hydrogen production, has attracted more and more research attentions[2]. However, due to the unsuitable adsorption/desorption capacity of the reaction intermediates (H^*, O^*), it is difficult for the reaction intermediates to desorb from the catalyst surface to form the final product, which seriously hinders the progress of the reaction[3,4]. Although researchers have made significant progress in the design of catalysts, a large cell voltage is still needed to drive this process. Therefore, it is still highly desirable to design high-efficiency water splitting electrocatalysts.

Recently, ruthenium (Ru) has attracted special attention for water splitting catalysis since its inherently excellent activity and far lower price than platinum (Pt) and iridium (Ir)[5-9]. To date, various strategies have been applied to enhance the activity of the Ru-based catalysts, including turning the crystal phase, doping electrocatalysts with hetero atoms, alloying Ru with the transition metals, and so on forth[7,10,11]. In principle, since the electrocatalysis is usually carried out on the surface of a catalyst, controlling the surface structure of the catalyst

is a more straightforward way to improve the catalytic performance. The high-index crystal facets have more coordination unsaturated atoms and more active sites, which is believed to be more active[12-14]. Nevertheless, there were fewer reports on controlling the Ru-based catalysts with high-index facets. To this end, the fine control of Ru-based catalysts is of great significance in both practical application and fundamental research.

Herein, we have successfully created a unique class of RuCo nanoscrews (NSs) for water electrosplitting with high efficiency by exposing high-index facet. The RuCo NSs exhibited excellent HER (18 mV @ 10 mA cm^{-2}) and OER (231 mV @ 10 mA cm^{-2}) activity in alkaline solution. It was further demonstrated that the RuCo NSs can be adopted as bifunctional overall water splitting electrocatalysts with a low cell voltage of 1.524 V and stability of up to 20 h. Mechanism studies show that the RuCo NSs can effectively reduce the energy barrier of water dissociation, regulate the adsorption and desorption of intermediates, and thus accelerating the whole reaction. Density functional theory (DFT) calculations reveal that the local RuCo NS lattice strain mapping disorder mostly localizes at the apex of ridges and edges regions. Within these regions, low coordinated Ru- and Co- sites play crucial roles in efficient and robust electronic exchange and transfer (EXT) between adsorbing sites and intermediates. With this trend, the NS system not only lowers the initial H_2O activation energy level but also alleviates the barrier of H-O-H scissoring. From views of both electronic and energetic activities, high-performance water-splitting catalysis has been guaranteed.

The RuCo NSs were prepared by a simple wet-chemical reaction, in which $RuBr_3$ and $Co(acac)_3$ were selected as the metal precursors. We initially characterized the morphology and structure of the prepared RuCo nanocrystals. High-angle annular dark-field scanning transmission electron microscopy (HAADF-STEM) (**Figure 1a**) image review that the RuCo nanocrystals are highly dispersive with a uniform size distribution of average length of ~31

nm and average diameter of ~6 nm (**Figure 1b**). As observed in the HAADF-STEM image, the RuCo NSs have a rough surface with nanoscrew-like profile, thus, naming RuCo nanoscrews (RuCo NSs). The atomic ratio of Ru/Co is 59.45/40.55, as revealed by energy-dispersive X-ray spectroscopy (EDS) (**Supplementary Figure 1a**). STEM-EDS elemental mappings were used to investigate the elemental distribution of RuCo NSs (**Figure 1c**), where the Ru and Co uniformly distributed crossing the crystal. As confirmed by the powder X-ray diffraction (PXRD) (**Supplementary Figure 1b**), the RuCo NSs can be indexed to the hexagonal closed-packed (*hcp*) crystal structure. Compared with pure Ru (JCPDS No. 06-0663), the {002} and {101} peaks of RuCo NSs were close to the peaks of the RuCo alloy (JCPDS No. 65-8976). Furthermore, the peak at 42.55° of RuCo NSs show a significantly enhanced diffraction peak belonging to the {002} plane, where the relative intensity ratio of the {002}/{101} (I_{002}/I_{101} = 0.805) is much larger than the standard values in the JCPDF cards of Ru (No. 06-0663, I_{002}/I_{101} = 0.35) and RuCo (No. 65-8976, I_{002}/I_{101} = 0.268) (**Supplementary Figure 1c**), indicating that the preferential orientation in [002] direction of the crystal[15]. The lattice spacing of RuCo NSs is much closer to the RuCo (JCPDS No.65-8976) compared with Ru (JCPDS No. 06-0663), revealing the alloy structure[16].

To better decode the structure, the RuCo NSs were further characterized by details. The selected area electron diffraction (SAED) pattern (**Figure 1d**) further confirmed the *hcp* structure of the single crystalline of RuCo NSs, in agreement with the diffraction pattern from the [100] zone axis of Ru (*P63/mmc*) (**Supplementary Figure 2**)[17-19]. The atomic-resolution TEM image clearly shows the highly crystalline structure of RuCo NSs along the view of [100] zone axis with the *hcp* crystal structure (**Figure 1e**), in which the predominantly exposed crystal lattices spacing are determined to be 0.208 nm and 0.201 nm and can be attributed to the {002} and {101} planes and with many steps and edges. Both the 3D HAADF-STEM surface plot image (**Figure 1f**) and the magnified aberration-corrected

HAADF-STEM images of the RuCo (**Figure 1g and Supplementary Figure 3**) clearly show that the nanocrystals with rough surfaces with many steps and edges, and the corresponding fast Fourier transform (FFT) pattern (**Figure 1g, inset**) also confirmed the *hcp* phase structure.

To explore the effect of the unique structure of RuCo NSs on electrocatalysis, we first evaluated the HER performance of the catalysts in 1 M KOH at room temperature. Commercial Pt/C, RuO_2 and RuCo nanoparticles (NPs) (**Supplementary Figure 4**) were measured for comparison. As shown in **Figure 2a**, RuCo NSs demonstrate an overpotential of only 26 mV to reach 10 mA cm^{-2}, which is better than the RuCo NPs (33 mV), commercial Pt/C (57 mV) and RuO_2 (179 mV). Furthermore, the RuCo NSs achieve a large current of 48.34 mA cm^{-2} at the overpotential of 50 mV, which is 2.41 times higher than RuCo NPs (20.07 mA cm^{-2}) and 7.05 times higher than Pt/C (6.85 mA cm^{-2}), indicating the superior HER activity of RuCo NSs. The corresponding Tafel slope of RuCo NSs was calculated as 26.3 mV dec^{-1}, which is much smaller than that of RuCo NPS (29.4 mV dec^{-1}), Pt/C (39.5 mV dec^{-1}) and RuO_2 (101 mV dec^{-1}), suggesting the more efficient HER kinetics (**Figure 2b and Supplementary Figure 5a**)[20]. To reveal the intrinsic activity of the catalysts, TOF values were calculated to reveal the intrinsic HER activity. Cu-UPD was used to estimate the active sites of all catalysts (**Supplementary Figure 6**)[21]. As we observed in **Supplementary Figure 7**, RuCo NSs achieve the highest TOF value (8.4 H_2 s^{-1}) at the overpotential of 50 mV in 1 M KOH, which are much higher than those of Pt/C (1.32 H_2 s^{-1}) and other reported (HER) catalysts, further revealing the superior catalytic performance of RuCo NSs towards HER[21-25]. We further evaluated the intrinsic activity of different catalysts by normalizing the mass of Ru (mass activity) (**Supplementary Figure 8**)[26], where the mass activity values are 2556.6 A g^{-1}_{Ru} and 639.2 A g^{-1}_{Ru} at the overpotential of 50 mV of RuCo NSs and RuCo NPs, respectively (**Figure 2c and Supplementary Figure 9a**). OER performance of RuCo NSs was also tested

in 1 M KOH, RuCo NPs, RuO_2 and the commercial Ir/C were selected as references. As we observed in **Figure 2d**, RuCo NSs require a low overpotential of 231 mV to reach 10 mA cm^{-2}, much lower than those of the RuCo NPs (296 mV @ 10 mA cm^{-2}), RuO_2 (362 mV @ 10 mA cm^{-2}) and Ir/C (343 mV @ 10 mA cm^{-2}). Meanwhile, the corresponding Tafel slope of RuCo NSs was calculated as 86.8 mV dec^{-1}, smaller than those of RuCo NPs (92.4 mV dec^{-1}) RuO_2 (104 mV dec^{-1}) and Ir/C (98 mV dec^{-1}), clearly demonstrating the enhanced kinetics of RuCo NSs towards OER (**Figure 2e and Supplementary Figure 5b**)[27]. The mass activity values are 3366.9 A g^{-1}_{Ru} and 572.3 A g^{-1}_{Ru} at the overpotential of 50 mV of RuCo NSs and RuCo NPs, respectively (**Figure 2f and Supplementary Figure 9b**)[26]. All these results demonstrate that the unique structure of RuCo NSs with high-index facets considerably improved the intrinsic activity of the catalysts (**Supplementary Table 1-2**). Chronopotentiometry measurement was further used to evaluate the stability of RuCo NSs. As we observed in **Supplementary Figure 10-12**, RuCo NSs also exhibit superior stabilities for both HER and OER compared with commercial Pt/C and Ir/C. It is worth noting that the increase in the proportion of metal states on the surface of RuCo NSs can be attributed to the reduction potential of HER.

Given that the RuCo NSs have demonstrated promising activity and stability towards HER and OER, we further investigated the RuCo NSs as the bifunctional catalysts for overall water splitting. **Figure 2g** describes the polarization curves of RuCo NSs couple and Ir/C-Pt/C couple in 1 M KOH. It is worth noting that, RuCo NSs couple requires a low cell voltage of 1.524 V (@ 10 mA cm^{-2}) and excellent stability for more than 20 h (@ 10 mA cm^{-2}) with negligible degradation. On the contrary, the Ir/C-Pt/C couple exhibits lower performance (1.63 V @ 10 mA cm^{-2}) and poor stability for less than 10 h @ 10 mA cm^{-2} (**Figure 2h**)[28]. According to the TEM image, STEM-EDS mappings and X-ray photoelectron spectroscopy (XPS) spectra, RuCo NSs show no obvious morphology and composition change after water

splitting stability test, confirming the excellent catalytic stability (**Supplementary Figures 13-15**).

To get a fundamental understanding of the high performance of RuCo NSs, the surface electron structure of the RuCo NSs and RuCo NPs was investigated by XPS. As we observed in the Ru 3p region (Figure 3a), the peaks located at ~463 eV and ~467 eV correspond to the Ru^0 $3p_{3/2}$ and Ru^{4+} $3p_{3/2}$, demonstrating the coexistence of metallic state and oxidized state of Ru in the RuCo NSs[29,30]. As for Co, the Co 2p region also reveals that coexistence of Co^{2+} (Co^{2+} $2p_{1/2}$: 796.4 eV, Co^{2+} $2p_{3/2}$: 780.4 eV) and Co^{3+} (Co^{3+} $2p_{1/2}$: 798.8 eV, Co^{3+} $2p_{3/2}$: 782.5 eV) (**Figure 3b**)[31,32].

The soft X-ray absorption spectrum at the Co-$L_{2,3}$ edges is highly sensitive to the valence and the local environment of Co ions.[33-36] Here, we explore the electronic structure at the surface layers using a surface sensitive total electron yield mode (TEY) (~2nm,) and the elative deep inside of the particles using a self-absorption-free bulk sensitive partial fluorescence yield mode (IPFY).[37,38] As shown in **Figure 3c** the Co-L_3 spectrum of RuCo NSs taken with IPFY mode exhibits a broad structure-less peak like Co metal, while the spectrum collected with TEY mode presents the multiple spectral feature similar to that of CoO. Thus, our Co-L_3 XAS spectra demonstrate an oxidized shell and metallic core of RuCo NSs and a situation known in CoO/Co core-shell system known previously.[39]

X-ray absorption near-edge structure (XANES) and the extended X-ray absorption fine structure (EXAFS) are also sensitive to the electronic structure and the local environment of metal ion.[40-43] The Ru K-edge normalized absorption spectrum of XANES (**Supplementary Figure 16**) shows that Ru in RuCo NSs appears to be in the middle valence state of RuO_2 and Ru foil indicating also partially oxidized Ru similar to the situation of Co ion. We further

examined the bond structure of Ru by the Fourier transform of the EXAFS (FT-EXAFS) spectrum. As shown in **Figure 3d**. The peaks located at 1.47 Å and 3.13 Å are associated with the Ru-O bond and Ru-Ru bond of the RuO_2, respectively.[11,44] In the curves of Ru foil, the main Ru-Ru coordination is located at 2.39 Å. It is worth noting that the peak of RuCo NSs is around 1.78 Å, which is between the Ru-O and Ru-Ru bonds. This is due to the coordination of Ru with surrounding heteroatoms (Ru-Co, Ru-O and Ru-Ru bonds) (**Supplementary Figure 17 & Supplementary Table 3**). In order to further explore the effect of the coordination structure of RuCo NSs, we used the wavelet transforms (WT) of the Ru K-edge EXAFS to obtain the radial distance resolution in K-space. As shown in **Supplementary Figure 18**, the WT contour plot of RuCo NSs exhibits a maximum at the interatomic distance of about 3.6 Å, which can be considered as the influence of the preferred orientation[45]. In addition, the slight displacement of RuCo NSs in the K space around 8.9 $Å^{-1}$ is due to the synergistic effect of the heteroatoms around Ru. We further used operando XANES to investigate the true active sites of RuCo NSs during the OER measurement. As shown in **Supplementary Figure 19**, compared with the open circuit potential (OCP), Co K-edge shows no change under the applied potential of 1.5 V vs. RHE. In contrast, Ru K-edge shifts to higher energy about 1.0 eV from OCP to 1.5 V, indicating Ru is the active site during the OER measurement.

To better understand these oxidation states, the O 1s XPS of the RuCo NSs and RuCo NPs were further measured. As shown in **Figure 3e**, three different oxygen species were observed in O 1s spectra. The peaks located at 530.1, 532.1, 533.7 eV can be attributed to lattice oxygen (RuO_2), hydroxyl group (Ru-OH) and adventitious species, respectively[46]. Previous works have reported that the lattice oxygen species of Ru exhibits a weak binding capacity to the intermediate species in the reaction, while the surface hydroxyl species (Ru−OH) are considered to possess high adsorption with oxygen species. Compared with RuCo NPs, the

proportion of surface hydroxyl species (Ru-OH) on the RuCo NSs increases, indicating that RuCo NSs have a much stronger bonding with the adsorption species (H_2O). In general, the rate-limiting step of HER in alkaline solution is the water dissociation of the Volmer step ($H_2O + e^- \rightarrow H^* + OH^-$, where * denotes the site on the electrode surface)[11]. Thus, the cleavage of the HO-H bond plays an important role in the rate of the reaction. Above all, the RuCo NSs have a faster adsorb of H_2O and would accelerate the water dissociation. Water splitting involves two reactions, wherein OER is a process involving multiple adsorption/desorption intermediates (HO^*, O^*, HOO^*) of the reaction, and the rate-limiting step is the formation of HOO^* from O^*. Therefore, O^* should have a moderate adsorption/desorption capacity on the catalyst surface, which should not be too strong or too weak[47]. Based on the volcano plot, Ru is too weak for O^*, while Co has a strong adsorption capacity for O^*[47]. Thus, according to the XPS analysis, the introduction of Co can adjust the *d*-band electron of Ru, balancing the adsorption and desorption of O^*, which is beneficial to the reaction. These results well validate the conclusions of the valence band of RuCo NSs (**Figure 3f**), in which the *d*-band of the RuCo NSs is -1.190 eV, which upshifts than that for the RuCo NPs (-1.305 eV), revealing that the RuCo NSs have a more suitable binding ability with the reaction intermediates than RuCo NPs, ultimately facilitating the kinetics of the reaction[48,49].

We are now interpreting the excellent HER and OER performances within alkaline conditions. To be consistent with the experimental characterizations, the RuCo (0001) surfaces have been cleaved within the hexagonal close packing lattice of RuCo lattice. Based on experimental characterizations, many steps and edges have been noticed on the {002} and {101} planes on the surface, which have been assigned to different high index surfaces. Accordingly, the structural model has been built with consideration of the co-existence of lower coordinated edge apex and ridges, as well as convex-and-concave character (**Figure**

4a). The real space contour plots of active bonding and antibonding orbitals near the Fermi level (E_F) demonstrate the clear comparison of active electronic distributions (**Figure 4b and c**). The distribution contrast indicates, the electronic orbitals are less rich on the flat RuCo (0001) surface (**Figure 4b**). While the distribution turns to be more electron-rich character at the edge apex region and ridge area. Such contrasting electron-rich feature denotes a high probability of agglomerations for active sites or regions (**Figure 4c**). Owing the difficulties of reproducing the exact same structure of the nanoscrew, we have selected the nanostructure with evident edge and step feature to enlarge the strain induced in these regions through the MD simulations. From the surface strain mapping contour, the structural fluctuations are easily formed in terms of ridges and edge apexes near the middle part (**Figure 4d**). This arises because of the uneven strain mapping distributions with size exceeded beyond 15 nm. Meanwhile, the unit size of forming the twisting screw becomes more uniform (**Figure 4e**).

The PDOSs of the Ru-4d bands on various coordinated Ru-sites have been studied. With compared, the lower coordinated Ru-sites from CN = 8 to CN = 4 demonstrate the much more evident overlapping effect with E_F. The corresponding Ru-4d band centers have been also shifted towards the higher level close to E_F from E_V-2.1 eV to E_V-0.7 eV. Such a trend indicates lower coordinated Ru-sites staying at ridges, edges, and apex regions exhibit substantially high electronic activity for election transfer with O-species, supporting the experimental EXAFS results (**Figure 4f**). On the contrast, for the Co-sites with medium CN (from CN = 8 to CN = 6), the Co-3d band center demonstrated a nearly fixed band center staying at E_V-1.2 eV. We find most of these Co-sites locate at the regions of ridges and edges. Accordingly, these Co-3d bands have nearly been pinned indicating robust electronic exchange and transfer (EXT) between adsorbing species and nearby lattice sites (**Figure 4g**). We compared the TDOSs on the overall d-band contribution between NSs and (0001) surface. These are not only exhibiting the overall electronic activity trend but also efficiently

projecting out the essential difference between NS and uniform (0001) surface (**Figure 4h**). As shown in **Figure 4i**, from the initial H_2O adsorption to the formation of the O_2, we observe the linear correlation in the dominant peak of O-2p orbitals in different O-containing species. Regarding the 2p-band variation trend for the O-species, there have been found two linear trends from the H_2O towards the formation of O_2, where the dominant O-2p peak shifts towards the higher position and become closer to the Fermi level (E_F), indicating an efficient electron transfer towards the oxidation process. These confirm the high efficiencies of electron-transfer during the 4-electron H_2O oxidation (**Figure 4i**). For the intrinsic stress and strain, there has been a drastic stress-vibration discovered at the size below about 5 nm, where the lattice stress overall exhibits a shrinking trend towards the minimum at 4.9 nm. With the size increasing, the stress turns to be stabilized approaching equilibrium (**Figure 4j**). The mapping of the strain further indicates the existence of strain on the edge and step region (**Supplementary Figure 20a-b**). Meanwhile, the slight distortion of the RuCo nanoparticle after MD simulations further confirm the strain effect (**Supplementary Figure 20c-d**). Our further mapping of the intrinsic size-dependent lattice strain reflects the distribution. We find the near linear-scale downtrend for the lattice from shrinking behavior crossover the 15 nm borderline, towards possible NS formation by intrinsic fringe shrinking effect (**Figure 4k**).

We further move on to the energetic pathways to interpret the HER and OER energy properties (**Figure 5**). For the alkaline HER, the pathway given from the NS system not only lowers the initial adsorption energy level for [*H + H_2O*], but also alleviates the barrier of forming the [2H + HO*]. Accordingly, the resulted formation of [H_2 + HO*] within the RuCo NS system shows more energetically favorable than the one found in the flat (0001) surface (**Figure 5a**). Further transition state barrier analysis confirms alkaline HER performance arises because the H_2O-splitting step exhibits nearly half of the barrier height (0.25 eV vs. 0.53 eV) for RuCo NS compared to (0001) surface (**Figure 5b**). We further move onto the

OER pathways within alkaline conditions, focusing on the RuCo NS system. It shows that under U = 0 V standard potential, alkaline OER pathways are energetically favorable, and potential determining step occurred at the formation of [*OOH^-] staying at the level near 3.90 eV. This character arises from the prominent electron-transfer of highly active Ru-sites as well as a robust valence state of Co-site with 3d-band pinned (**Figure 5c**). At the potential of U=1.23 V, the evident energetic difference has been presented. The alkaline pathway possesses a lower overpotential height for overcoming the barrier of forming [*OOH^-]. Therefore, the RuCo NS system exhibits high performance in alkaline OER catalysis (**Figure 5d**). Overall, from both electronic activities and energetic pathways analysis, we confirm that, the synergetic contributions from both extra-low coordinated Ru- and Co- sites substantially facilitate the competitively full water splitting catalytic performance for efficient HER and OER simultaneously.

In conclusion, we have designed a new class of RuCo NSs for efficient overall water electrosplitting. Aberration-corrected HAADF-STEM reveals that the RuCo NSs with rough surfaces expose many edges and steps. The RuCo NSs exhibit superior activity for HER (26 mV @ 10 mA cm^{-2}) and OER (231 mV @ 10 mA cm^{-2}). Significantly, the RuCo NSs also exhibit low cell voltage of 1.524 V (@ 10 mA cm^{-2}) as bifunctional water splitting electrocatalyst and excellent stability for more than 20 h (@ 10 mA cm^{-2}). The enhanced activity of RuCo NSs is due to the optimization of the binding energy with the intermediate species in the water splitting reaction. DFT calculations reveal that, the intrinsic lattice strain deviation induces morphological NS formation for RuCo system. Such a structural character endows the amount of low coordinated Ru- and Co- sites, which plays a facilitating role in the electronic exchange and transfer with intermediates transformation during H_2O splitting. Within this trend, the local CN disordered Ru and Co sites not only lowers the initial adsorption barrier of H_2O but also minimizes the transition barrier for H-O-H bond scissoring,

promoting the electron-lattice coupling effect. This work paves new prospects for the design of efficient electrocatalysts for overall water splitting.

Experimental Section

Chemicals: Ruthenium(III) bromide ($RuBr_3$, 99%) was purchased from Alfa Aesar. Ruthenium Carbonyl ($Ru_3(CO)_{12}$, ≥ 98%), cobalt(III) acetylacetonate ($Co(acac)_3$, 98%), oleylamine ($CH_3(CH_2)_7CH=CH(CH_2)_7CH_2NH_2$, OAm, >70%), polyvinylpyrrolidone ($(C_6H_9NO)_n$, PVP, average M.V. 58000) and L-ascorbic acid ($C_6H_8O_6$, 99%) were purchased from J&K Scientific (Beijing, China). Hydroquinone ($C_6H_6O_2$, AR, ≥ 99.0%), potassium hydroxide (KOH, AR, ≥ 85%), ethylene glycol ($C_2H_6O_2$, EG, AR, ≥ 99.5%), cyclohexane (C_6H_{12}, AR, ≥ 99.7%), ethanol (C_2H_6O, AR, ≥ 99.7%), isopropanol (C_3H_8O, AR, ≥ 99.7%) and sulfuric acid (H_2SO_4, AR, 95%-98%) were purchased from Sinopharm Chemical Reagent Co. Ltd. (Shanghai, China). Vulcan XC-72 R carbon black was purchased from Cabot. Commercial Pt/C (20% Pt on XC-72R) and commercial Ir/C (20 Ir on XC-72R) were purchased from Johnson Matthey (JM) Corporation (with the minimum metal surface area of 90 m^2 g^{-1}, maximum crystal size of 3.5 nm). Ruthenium (IV) oxide (RuO_2) was purchased from Sigma-Aldrich. All the chemicals were used as received without further purification. The water (18 MΩ/cm) used in all experiments was prepared by passing through an ultra-pure purification system (Aqua Solutions).

Synthesis of RuCo NSs: In a typical preparation of RuCo NSs, $RuBr_3$ (8.5 mg), $Co(acac)_3$ (6 mg), hydroquinone (55 mg) and OAm (5 mL) were added into a vial (volume: 35 mL). After the vial had been capped, the mixture was ultrasonicated for around 15 min. The resulting homogeneous mixture was then heated from room temperature to 230 °C in 30 min and maintained for 5 h in an oil bath before it was cooled to room temperature. The RuCo NSs were collected by centrifugation and washed three times with cyclohexane/ethanol mixture.

Synthesis of RuCo NPs: In a typical preparation of RuCo NPs, $Ru_3(CO)_{12}$ (5.4 mg), $Co(acac)_3$ (6 mg), L-ascorbic acid (54.6 mg), PVP (40 mg) and EG (10 mL) were added into a vial (volume: 35 mL). After the vial had been capped, the mixture was ultrasonicated for around 15 min. The resulting homogeneous mixture was then heated at 180 °C for 5 h before it cooled down to room temperature. The RuCo NPs were collected by centrifugation and washed three times with acetone/ethanol mixture.

Characterization: The samples were prepared by dropping cyclohexane or ethanol dispersion of samples onto carbon-coated copper TEM grids using pipettes and dried under ambient conditions. Low-magnification transmission electron microscopy (TEM) was conducted on a HITACHI HT7700 transmission electron microscope at an accelerating voltage of 120 kV. High-resolution TEM (HRTEM) and scanning TEM (STEM) were conducted on an FEI Tecnai F20 transmission electron microscope at an accelerating voltage of 200 kV. HRTEM, STEM and high-angle annular dark-field STEM energy-dispersive X-ray spectroscopy (HAADF-STEM-EDS) were conducted on a JEOL GrandARM300F scanning transmission electron microscope with double Cs correctors at an acceleration voltage of 300 kV. Powder X-ray Diffraction (PXRD) pattern was collected on X'Pert-Pro MPD diffractometer (Netherlands PANalytical) with a Cu Kα X-ray source (λ = 1.540598 Å). The concentration of catalysts was determined by the inductively coupled plasma optical emission spectrometer (Varian 710-ES). X-ray photoelectron spectra (XPS) was collected with an SSI S-Probe XPS Spectrometer. The Co-L_3 and Ru-K XAS spectra were collected at the TLS-BL20A and TPS-BL 44A, respectively of the National Synchrotron Radiation Research Center (NSRRC, Hsinchu, Taiwan). The Ru-*K* EXAFS Data were processed according to standard procedures using the Demeter program package (Version 0.9.24)[50]. TGA was performed on SII TG/DTA 6300 thermogravimetric analyzer over a temperature range of 25-900 °C at a heating rate of 10 °C min^{-1} in oxygen atmosphere.

Electrochemical Measurement: For all the electrochemical tests, a three-electrode system was used to conduct the electrochemical measurements at an electrochemical workstation (CHI 660E). To prepare the working electrode, RuCo NSs or RuCo NPs were loaded on carbon powder (Vulcan XC-72 R, Cabot) in 10 mL ethanol and sonicated for 0.5 h to deposit NSs on carbon. The products were separated by centrifugation and washed with ethanol/acetone three times, and then annealed in air at 250 ºC for 1 h. Finally, the catalyst (2.0 mg) was dispersed in 390 μL water-ethanol solution (3:1, v/v) and 10 μL 5 wt% Nafion by ultrasonicating for 1 h to form a homogeneous ink. 10 μL catalyst ink was then loaded onto a glassy carbon electrode (GCE, diameter: 5 mm, area: 0.196 cm^2). The mass loading of the catalyst was 0.25 mg/cm^2. A graphite rod and a saturated calomel electrode (SCE) were used as counter electrode and the reference electrode, respectively. The reference was calibrated with respect to the reversible hydrogen electrode (RHE). Linear sweep voltammetry (LSV) was carried out at 5 mV s^{-1} at room temperature. For comparison, the commercial Pt/C and Ir/C were examined in all tests under the same conditions.

Active Sites Calculations: The number of active sites (n) can be qualified based on the underpotential deposition (UPD) copper stripping charge (Q_{Cu}, $Cu_{UPD} \rightarrow Cu^{2+} + 2e^-$) with the following formula:

$$n = Q_{Cu} / 2F \quad (1)$$

where F is the Faraday constant (C mol^{-1})[21].

Turnover Frequency (TOF) Calculations: TOF was calculated using the following formula:

$$TOF = I / (2Fn) \quad (2)$$

where I is the current (A) during the linear sweep measurement, F is the Faraday constant (C mol^{-1}), n is the active sites (mol)[21].

Computational Details: We have carried out the simple DFT calculations based on the CASTEP code[51]. The overall geometric optimization has also been considered, where the algorithm of Broyden-Fletcher-Goldfarb-Shannon (BFGS) has chosen for all related geometry

optimization calculations. The plane-wave basis set for expressing the valence electronic states has been used with a kinetic cutoff energy of 750 eV. The PBE functional has been set for the calculations. During electronic-minimization process, the ensemble DFT (EDFT) method of Marzari et al[52]. is used to guarantee the convergence and avoid the spin-charge sloshing effect.

For DFT electronic structure calculations and energetic pathway analysis, regarding the balance of structural modeling and computation demanding cost, we consider the model has been built based on the RuCo (0001) surface within hexagonal close packing lattice. The RuCo NS particle has been established through axially twisted by randomized angles for each atomic layer in size of 160 atoms. Based on this structural framework, the vacuum thickness is set to the value larger than 15 Å in order to separate any two adjacent RuCo NS particles for lattice coupling. The separations are considered in terms of top surface, ridges, and edges. To balance the computational demanding cost, the Monkhost-Pack reciprocal space integration was performed using Gamma-center-off special k-points with mesh of 2×2×2, which was guided by the initial convergence test[53]. With these settings, the overall total energy for each step was converged to less than 5.0×10^{-7} eV per atom. The Hellmann-Feynman forces on the atom were converged to less than 0.001 eV/Å.

For the strain distribution, we applied the Large-scale atomic/molecular massively parallel simulator (LAMMPS) for MD simulations[54]. Sufficiently large cubic boxes are created to avoid thermal perturbations of a perfect lattice. This initial model has been build in a sufficiently large periodic cubic box to avoid the thermal perturbations of a perfect lattice. The atomic interactions have been modelled with the embedded-atom method. The system energy has been minimized first to reach the equilibrium configuration. The time-integration on Nose-Hoover style non-Hamiltonian equations of motion has been performed under the NVT condition (canonical ensembles) with a constant temperature of 10K and the MD duration time has been set to 3 ns to obtain the atom positions and velocity under the

configuration. The Verlet algorithm has been applied for the velocity to with an integration time step of 1.0 fs. The periodic boundary condition has been applied in x, y, and z three directions. We have selected the distinctive styles of the EAM potential for the MD simulations. The demonstration of stress per-atom during uniaxial tensile strain evolution is actualized by the OVITO package[55]. For mechanical properties analysis, we further use LAMMPS to investigate the atomic lattice stress and strain distribution of RuCo cluster with different sizes from 12000 to 100000 atoms, with a ratio of 3:2 for Ru:Co, respectively. The structures of the MD models are selected from the edge and steps of the RuCo nanoscrews, which aim to enlarge the mechanical properties difference in the edge and step region of the nanoscrew. We focus on the strain effect trend induced at the edge region, in which the two elements have been treated differently only in the potential field.

The Ru, Co, O, and H norm-conserving pseudopotentials are generated using the OPIUM code in the Kleinman-Bylander projector form, and the non-linear partial core correction and a scalar relativistic averaging scheme are used to treat the mixed valence (Fe, Ni) spin-orbital coupling effect[56-58]. We chose the projector-based (4*d,* 5*s*, 5*p*), (3*d,* 4*s*, 4*p*), (2*s*, 2*p*), and (1*s*) states to reflect the valence states of Ru, Co, O, and H atoms respectively. The RRKJ method is chosen for the optimization of the pseudopotentials[59].

Supporting Information
Supporting Information is available from the Wiley Online Library or from the author.

Acknowledgements
This work was financially supported by the Ministry of Science and Technology (2016YFA0204100, 2017YFA0208200), the National Natural Science Foundation of China (21571135, 21771156), the Young Thousand Talented Program, Jiangsu Province Natural Science Fund for Distinguished Young Scholars (BK20170003), the Priority Academic Program Development of Jiangsu Higher Education Institutions (PAPD), the start-up supports from Xiamen University and the Early Career Scheme (ECS) fund (Grant No.: PolyU 253026/16P) from the Research Grant Council (RGC) in Hong Kong.

Received: ((will be filled in by the editorial staff))
Revised: ((will be filled in by the editorial staff))
Published online: ((will be filled in by the editorial staff))

References

[1]. Roger, I., Shipman, M. A. & Symes, M. D. Earth-abundant Catalysts for Electrochemical and Photoelectrochemical Water Splitting. *Nat. Rev. Chem.* **1**, 0003 (2017).

[2]. Seh, Z. W. *et al.* Combining Theory and Experiment in Electrocatalysis: Insights into Materials Design. *Science* **355**, eaad4998 (2017).

[3]. Danilovic, N. *et al.* The Effect of Noncovalent Interactions on the HOR, ORR, and HER on Ru, Ir, and $Ru_{0.50}Ir_{0.50}$ Metal Surfaces in Alkaline Environments. *Electrocatalysis* **3**, 221-229 (2012).

[4]. Yu J, He Q, Yang G, Zhou W, Shao Z, Ni M. Recent Advances and Prospective in Ruthenium-Based Materials for Electrochemical Water Splitting. *ACS Catal.* **9**, 9973-10011 (2019).

[5]. Feibelman, P. J. Partial Dissociation of Water on Ru(0001). *Science* **295**, 99-102 (2002).

[6]. Andersson, K., Nikitin, A., Pettersson, L. G., Nilsson, A. & Ogasawara, H. Water Dissociation on Ru(001): An Activated Process. *Phys. Rev. Lett.* **93**, 196101 (2004).

[7]. Su, J. *et al.* Ruthenium-cobalt Nanoalloys Encapsulated in Nitrogen-doped Graphene as Active Electrocatalysts for Producing Hydrogen in Alkaline Media. *Nat. Commun.* **8**, 14969 (2017).

[8]. Creus, J. *et al.* Ruthenium Nanoparticles for Catalytic Water Splitting. *ChemSusChem* **12**, 2493-2514 (2019).

[9]. Han, S. *et al.* Metallic Ruthenium-based Nanomaterials for Electrocatalytic and Photocatalytic Hydrogen Evolution. *J. Mater. Chem. A* **7**, 24691-24714 (2019).

[10]. Li, W. Z. *et al.* Chemical Insights into the Design and Development of Face-Centered Cubic Ruthenium Catalysts for Fischer-Tropsch Synthesis. *J. Am. Chem. Soc.* **139**, 2267-2276 (2017).

[11]. Mao, J. *et al.* Accelerating Water Dissociation Kinetics by Isolating Cobalt Atoms into Ruthenium Lattice. *Nat. Commun.* **9**, 4958 (2018).

[12]. Bu, L. *et al.* A General Method for Multimetallic Platinum Alloy Nanowires as Highly Active and Stable Oxygen Reduction Catalysts. *Adv. Mater.* **27**, 7204-7212 (2015).

[13]. Zhang, Z. *et al.* Crystal Phase and Architecture Engineering of Lotus-Thalamus-Shaped Pt-Ni Anisotropic Superstructures for Highly Efficient Electrochemical Hydrogen Evolution. *Adv. Mater.* **30**, e1801741 (2018).

[14]. Perdew, J. P., Burke, K. & Ernzerhof, M. Generalized Gradient Approximation Made Simple. *Phys. Rev. Lett.* **77**, 3865-3868 (1996).

[15]. Luc, W. *et al.* Two-dimensional Copper Nanosheets for Electrochemical Reduction of Carbon Monoxide to Acetate. *Nat. Catal.* **2**, 423-430 (2019).

[16]. Liu, Y. *et al.* A General Route to Fabricate Low-ruthenium-based Bimetals Electrocatalysts for pH-universal Hydrogen Evolution Reaction *via* Carbon Quantum Dots. *Angew. Chem. Int. Ed.* **59**, 1718-1726 (2020).

[17]. Watt, J., Yu, C., Chang, S. L., Cheong, S. & Tilley, R. D. Shape Control from Thermodynamic Growth Conditions: The Case of hcp Ruthenium Hourglass Nanocrystals. *J. Am. Chem. Soc.* **135**, 606-609 (2013).

[18]. Lu, Q. *et al.* Crystal Phase-based Epitaxial Growth of Hybrid Noble Metal Nanostructures on 4H/fcc Au Nanowires. *Nat. Chem.* **10**, 456-461 (2018).

[19]. Jiang, R., Tran, D. T., Li, J. & Chu, D. Ru@RuO_2 Core-Shell Nanorods: A Highly Active and Stable Bifunctional Catalyst for Oxygen Evolution and Hydrogen Evolution Reactions. *Energy Environ. Mater.* 2, 201-208 (2019).

[20]. Voiry, D., Shin, H. S., Loh, K. P. & Chhowalla, M. Low-dimensional Catalysts for Hydrogen Evolution and CO_2 Reduction. *Nat. Rev. Chem.* **2,** 0105 (2018).

[21]. Mahmood, J. *et al.* An Efficient and pH-universal Ruthenium-based Catalyst for the Hydrogen Evolution Reaction. *Nat. Nanotechnol.* **12**, 441-446 (2017).

[22]. Liu, Y. *et al.* Ru Modulation Effects in the Synthesis of Unique Rod-like Ni@Ni_2P-Ru Heterostructures and Their Remarkable Electrocatalytic Hydrogen Evolution Performance. *J. Am. Chem. Soc.* **140**, 2731-2734 (2018).

[23]. Laursen, A. B. *et al.* Nanocrystalline Ni_5P_4: A Hydrogen Evolution Electrocatalyst of Exceptional Efficiency in Both Alkaline and Acidic Media. *Energy Environ. Sci.* **8**, 1027-1034 (2015).

[24]. McKone, J. R., Sadtler, B. F., Werlang, C. A., Lewis, N. S. & Gray, H. B. Ni-Mo Nanopowders for Efficient Electrochemical Hydrogen Evolution. *ACS Catal.* **3**, 166-169 (2013).

[25]. Ma, L., Ting, L. R. L., Molinari, V., Giordano, C. & Yeo, B. S. Efficient Hydrogen Evolution Reaction Catalyzed by Molybdenum Carbide and Molybdenum Nitride Nanocatalysts Synthesized *via* the Urea Glass Route. *J. Mater. Chem. A* **3**, 8361-8368 (2015).

[26]. Li, M. *et al.* Single-atom Tailoring of Platinum Nanocatalysts for High-performance Multifunctional Electrocatalysis. *Nat. Catal.* **2**, 495-503 (2019).

[27]. Yu, J. et al. Monoclinic $SrIrO_3$: An Easily Synthesized Conductive Perovskite Oxide with Outstanding Performance for Overall Water Splitting in Alkaline Solution. *Chem. Mater.* 32, 4509-4517 (2020).

[28]. Yu, J. et al. Spherical Ruthenium Disulfide-Sulfur-Doped Graphene Composite as an Efficient Hydrogen Evolution Electrocatalyst. *ACS Appl. Mater. Interfaces* 10, 34098-34107 (2018).

[29]. Yu, J. et al. Bigger is Surprisingly Better: Agglomerates of Larger RuP Nanoparticles Outperform Benchmark Pt Nanocatalysts for the Hydrogen Evolution Reaction. *Adv. Mater.* 30, 1800047 (2018).

[30]. Xu, Y. et al. Interface Effect of Ru-MoS_2 Nanoflowers on Lignin Substrate for Enhanced Hydrogen Evolution Activity. *Energy Environ. Mater.* DOI: 10.1002/eem2.12104 (2020).

[31]. Ling, T. *et al.* Engineering Surface Atomic Structure of Single-crystal Cobalt (II) Oxide Nanorods for Superior Electrocatalysis. *Nat. Commun.* **7**, 12876 (2016).

[32]. Liu, W. *et al.* A Highly Active and Stable Hydrogen Evolution Catalyst Based on Pyrite-structured Cobalt Phosphosulfide. *Nat. Commun.* **7**, 10771 (2016).

[33]. Chin, Y. Y. *et al.* Spin-orbit Coupling and Crystal-field Distortions for a Low-spin $3d^5$ State in $BaCoO_3$. *Phys. Rev. B* **100**, 205139 (2019).

[34]. Araújo, A. L., Maciel, R. P., Dornelas, R. G. F., Varjas, D. & Ferreira, G. J. Interplay Between Boundary Conditions and Wilson's Mass in Dirac-like Hamiltonians. *Phys. Rev. B* **100**, 205111(2019).

[35]. Guan, D. *et al.* Searching General Sufficient-and-Necessary Conditions for Ultrafast Hydrogen-Evolving Electrocatalysis. *Adv. Funct. Mater.* **29**, 1900704(2019).

[36]. Chen, J. M. *et al.* A Complete High-to-low Spin State Transition of Trivalent Cobalt Ion in Octahedral Symmetry in $SrC_{o0.5}Ru_{0.5}O_{3-\delta}$. *J. Am. Chem. Soc.* **136**, 1514-1519 (2014).

[37]. Yang, L. *et al.* Superiority of Native Vacancies in Activating Anionic Redox in P2-type $Na_{2/3}[Mn_{7/9}Mg_{1/9}\square_{1/9}]O_2$. *Nano Energy* **78,** 105172 (2020).

[38]. Tsai, H.-T. T. & Muan, A. Activity-Composition Relations in Refractory Oxide Solid Solutions at High Temperatures: The System Cr_2O_3-Al_2O_3. *J. Am. Ceram. Soc.* **75**, 1412-1415 (1992).

[39]. Ge, C. *et al.* Direct Observation of Rotatable Uncompensated Spins in the Exchange Bias System Co/CoO-MgO. *Nanoscale* **5**, 10236-10241 (2013).

[40]. Agrestini, S. *et al.* Nature of the Magnetism of Iridium in the Double Perovskite Sr_2CoIrO_6. *Physical Review B* **100**, 014443 (2019).

[41]. Chen, G. *et al.* Ultrahigh-performance Tungsten-doped Perovskites for the Oxygen Evolution Reaction. *J. Mater. Chem. A* **6**, 9854-9859 (2018).

[42]. Gu, J., Hsu, C. S., Bai, L., Chen, H. M. & Hu, X. Atomically Dispersed Fe^{3+} Sites Catalyze Efficient CO_2 Electroreduction to CO. *Science* **364**, 1091-1094 (2019).

[43]. Liu, H. *et al.* Insight into the Role of Metal-Oxygen Bond and O 2p Hole in High-Voltage Cathode $LiNi_xMn_{2-x}O_4$. *J. Phys. Chem. C* **121**, 16079-16087 (2017).

[44]. Kim, J. *et al.* High-Performance Pyrochlore-Type Yttrium Ruthenate Electrocatalyst for Oxygen Evolution Reaction in Acidic Media. *J. Am. Chem. Soc.* **139**, 12076-12083 (2017).

[45]. Hennig, C. *et al.* EXAFS and XRD investigations of zeunerite and meta-zeunerite. *Z. Kristallogr.* **218,** 37-45 (2003).

[46]. Abbott, D. F. *et al.* Iridium Oxide for the Oxygen Evolution Reaction: Correlation between Particle Size, Morphology, and the Surface Hydroxo Layer from Operando XAS. *Chem. Mater.* **28**, 6591-6604 (2016).

[47]. Wang, W., Xu, X., Zhou, W. & Shao, Z. Recent Progress in Metal-Organic Frameworks for Applications in Electrocatalytic and Photocatalytic Water Splitting. *Adv. Sci.* **4**, 1600371 (2017).

[48]. Shan, J., Ling, T., Davey, K., Zheng, Y. & Qiao, S. Z. Transition-Metal-Doped RuIr Bifunctional Nanocrystals for Overall Water Splitting in Acidic Environments. *Adv. Mater.* **31**, e1900510 (2019).

[49]. Zhao, Z.-J. *et al.* Theory-guided Design of Catalytic Materials Using Scaling Relationships and Reactivity Descriptors. *Nat. Rev. Mater.* **4**, 792-804 (2019).

[50]. Ravel B & Newville M. ATHENA, ARTEMIS, HEPHAESTUS: Data Analysis for X-ray Absorption Spectroscopy Using IFEFFIT. *J. Synchrotron Radiat.* **12**, 537-541 (2005).

[51]. Clark, S. J. *et al.* First Principles Methods Using CASTEP. *Z. Kristallogr.* **220**, 567-570 (2005).

[52]. Marzari, N., Vanderbilt, D. & Payne, M. C. Ensemble Density-Functional Theory for *Ab Initio* Molecular Dynamics of Metals and Finite-Temperature Insulators. *Phys. Rev. Lett.* **79**, 1337-1340 (1997).

[53]. Probert, M. I. J. & Payne, M. C. Improving the Convergence of Defect Calculations in Supercells: An *ab initio* Study of the Neutral Silicon Vacancy. *Phys. Rev. B* **67**, 075204 (2003).

[54]. Plimpton, S. Fast Parallel Algorithms for Short-Range Molecular Dynamics. *J. Comput. Phys.* **117**, 1-19 (1995).

[55]. Stukowski, A. Visualization and Analysis of Atomistic Simulation Data with OVITO-the Open Visualization Tool. *Model. Simul. Mater. Sc.* **18**, 015012 (2009).

[56]. Kleinman, L. & Bylander, D. M. Efficacious Form for Model Pseudopotentials. *Phys. Rev. Lett.* **48**, 1425-1428 (1982).

[57]. Louie, S. G., Froyen, S. & Cohen, M. L. Nonlinear Ionic Pseudopotentials in Spin-density-functional Calculations. *Phys. Rev. B* **26**, 1738-1742 (1982).

[58]. Grinberg, I., Ramer, N. J. & Rappe, A. M. Transferable Relativistic Dirac-Slater Pseudopotentials. *Phys. Rev. B* **62**, 2311-2314 (2000).

[59]. Rappe, A. M., Rabe, K. M., Kaxiras, E. & Joannopoulos, J. D. Optimized Pseudopotentials. *Phys. Rev. B* **41**, 1227-1230 (1990).

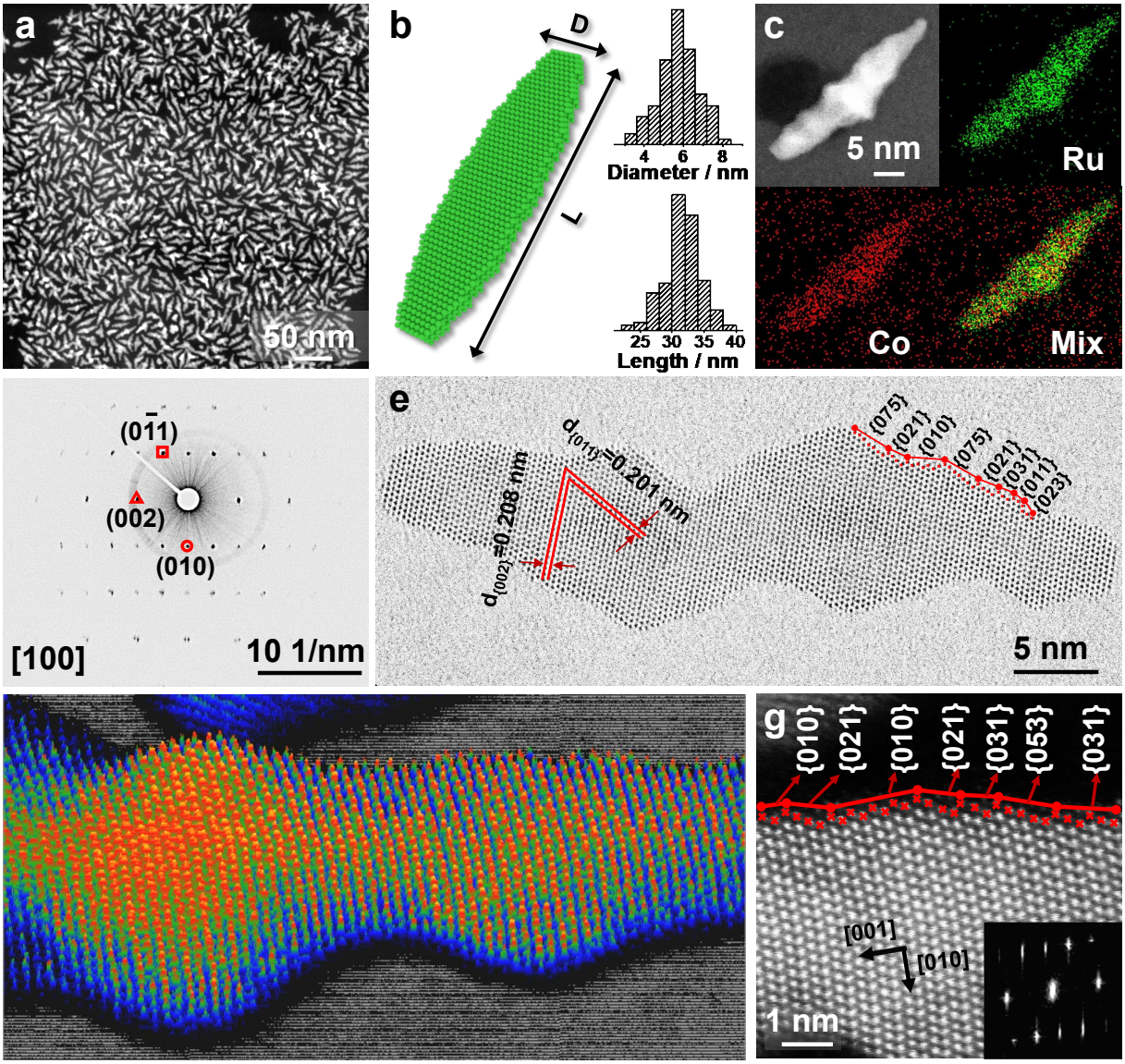

Figure 1. Morphology and structural characterization of RuCo NSs. (a) HAADF-STEM image, (b) diameter and length histograms, (c) STEM-EDS mappings, (d) SAED pattern (e) aberration-corrected HRTEM image, (f) 3D HAADF-STEM surface plot image and (g) aberration-corrected HAADF-STEM image (inset: corresponding FFT patterns) of RuCo NSs.

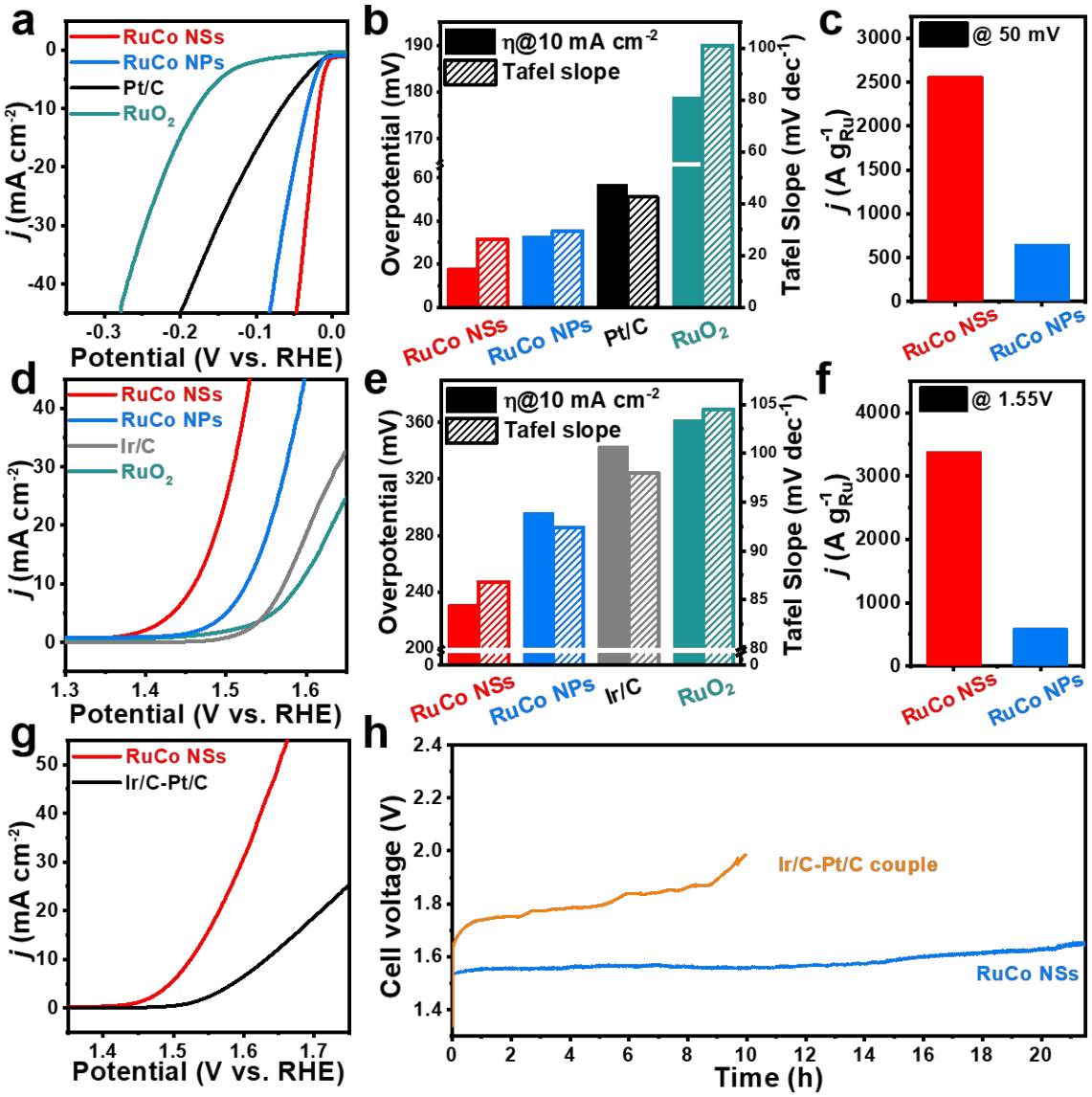

Figure 2. HER and OER performance of different catalysts. (a) HER polarization curves and (b) Tafel slopes of RuCo NSs, RuCo NPs, RuO_2 and Pt/C. (c) Mass activities of RuCo NSs and RuCo NPs for HER at overpotential of 50 mV. (d) OER polarization curves and (e) Tafel slopes of RuCo NSs, RuCo NPs, RuO_2 and Ir/C. (f) Mass activities of RuCo NSs and RuCo NPs for OER at potential of 1.55 V. (g) Overall water splitting performance and (h) chronopotentiometry stability measurements at 10 mA cm^{-2} of RuCo NSs and Ir/C-Pt/C couple in 1 M KOH.

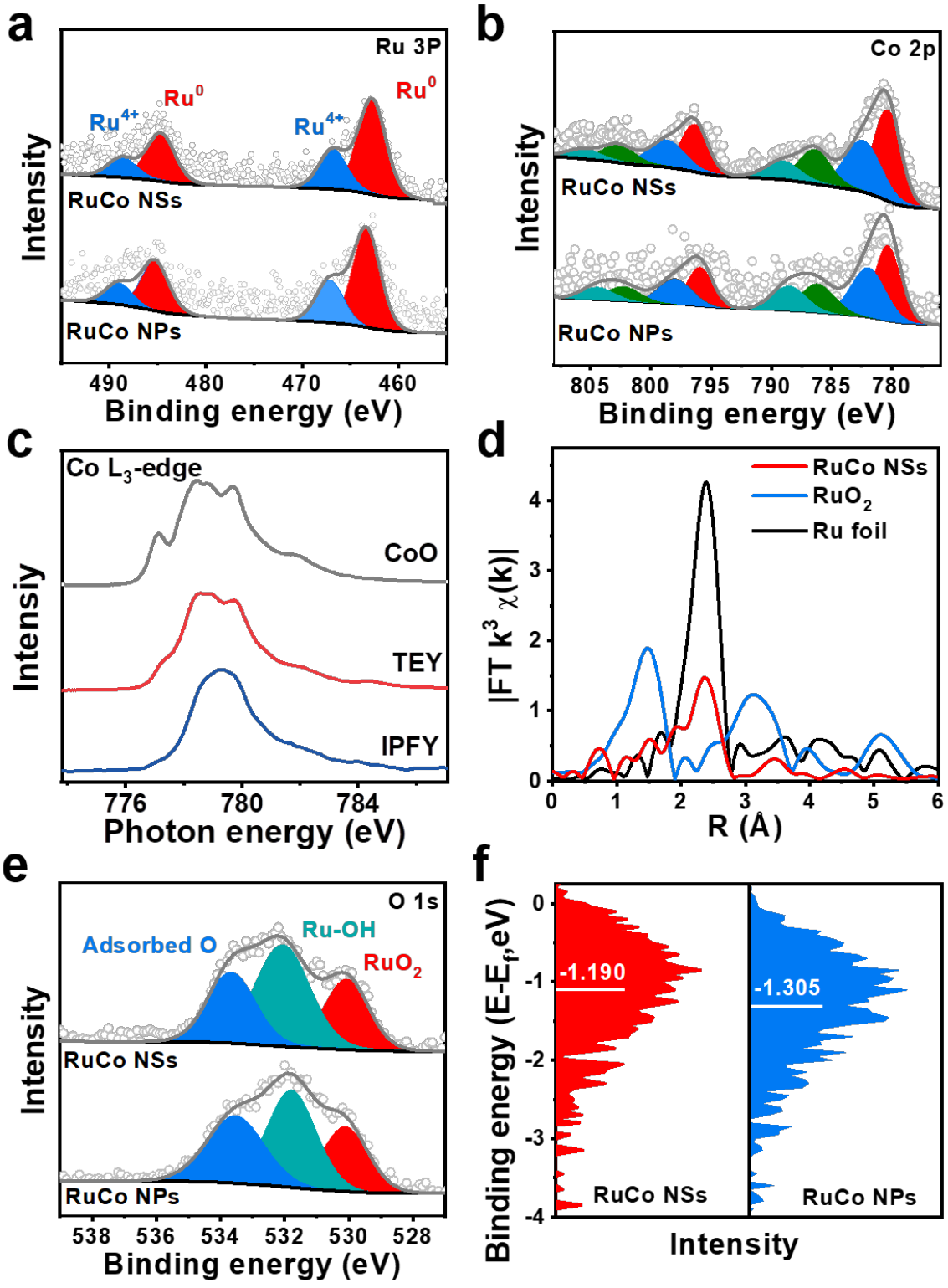

Figure 3. Surface characterization of RuCo NSs/C. XPS spectra of (a) Ru 3p, (b) Co 2p of RuCo NSs and RuCo NPs. (c) Co L_3-edge XAS spectra of CoO and RuCo NSs taken with TEY and IPFY modes. (d) Fourier transforms of Ru-K EXAFS spectra of RuCo NSs, RuO_2 and Ru foil. XPS spectra of (e) O 1s XPS of RuCo NSs and RuCo NPs. (f) Surface valence band photoemission spectra of RuCo NSs and RuCo NPs.

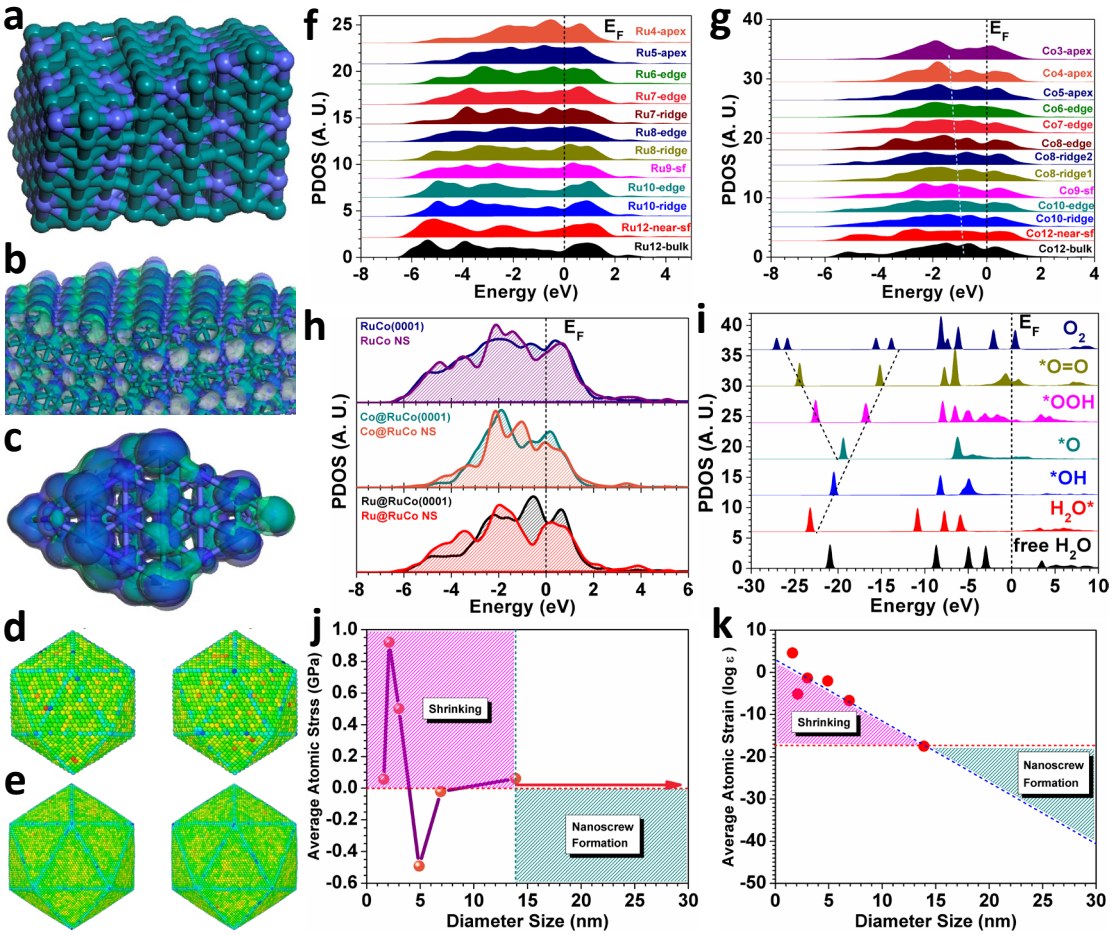

Figure 4. Electronic activities for HER and OER. (a) Local structural configuration of RuCo NS. (b) The real spatial 3D orbital contour plots of RuCo flat (0001) surface. (c) The real spatial 3D orbital contour plots of local fringe part of RuCo NS. (d) Transverse view of $Ru_{7200}Co_{4800}$ cluster with intrinsic lattice strain mapping. (e) Transverse view of $Ru_{60000}Co_{40000}$ cluster with intrinsic lattice strain mapping. (f) PDOSs of Ru-4d bands for different Ru-sites with different coordination number (CN). (g) PDOSs of Co-3d bands for different Co-sites with different CN. (h) TDOSs of overall and individual d-band contributions comparisons between RuCo NS and (0001) surface. (i) PDOSs of intermediate O-species of four-electron based acidic OER. (j) The average atomic stress evolution with the simulated cluster size. (k) The average atomic strain evolution with the simulated cluster size.

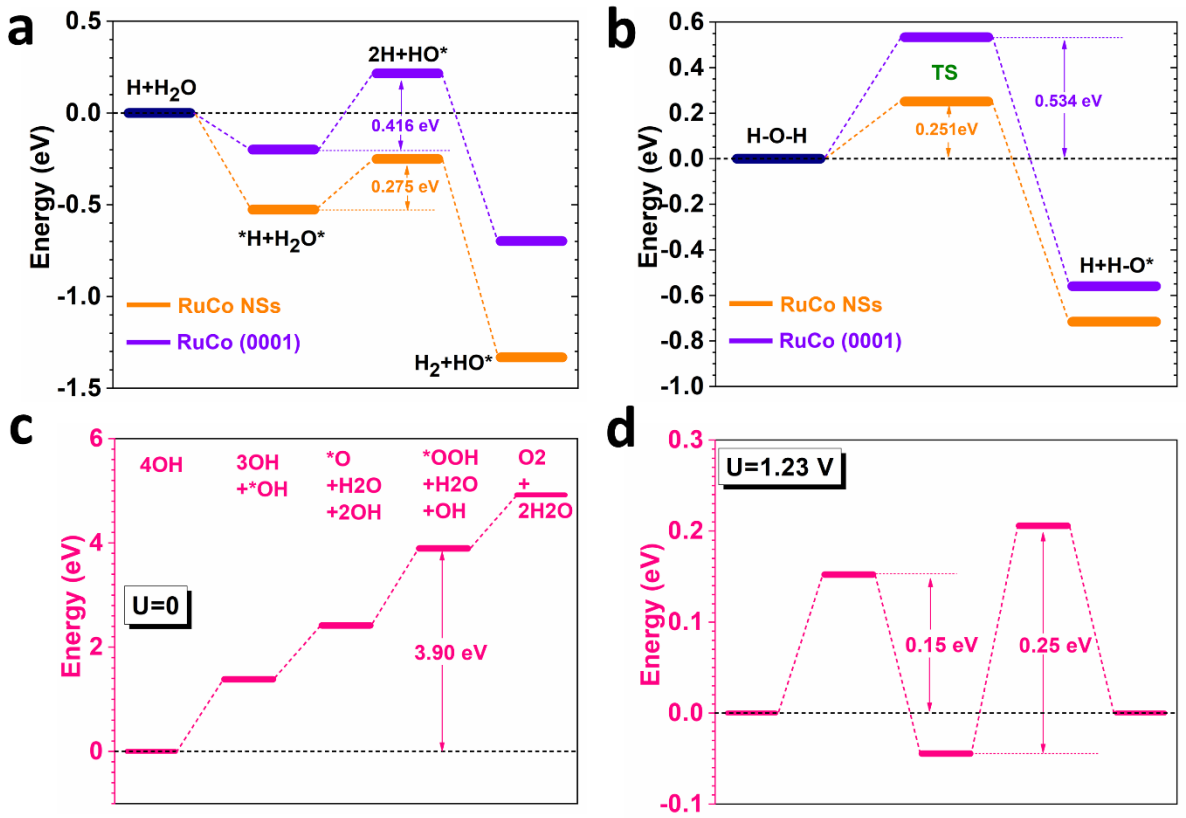

Figure 5. Energetic activities for HER and OER. (a) The pathway of alkaline HER occurred between RuCo NSs and (0001) surface systems. (b) The H_2O splitting energetic levels with transition state (TS) representing the splitting barrier. (c) The pathways of four-electron based alkaline OER at U=0 V. (d) The OER pathways are summarized at U=1.23 V.